28.2%-efficient, outdoor-stable perovskite/silicon tandem solar cells via improved phase stability

Jiang Liu[1*], *Erkan Aydin*[1], *Jun Yin*[2], *Michele De Bastiani*[1], *Furkan H. Isikgor*[1], *Atteq ur Rehman*[1], *Emre Yengel*[1], *Esma Ugur*[1], *George T. Harrison*[1], *Mingcong Wang*[1], *Yajun Gao*[1], *Jafar Iqbal Khan*[1], *Maxime Babics*[1], *Thomas G. Allen*[1], *Anand S. Subbiah*[1], *Kaichen Zhu*[3], *Xiaopeng Zheng*[2], *Wenbo Yan*[1], *Fuzong Xu*[1], *Michael F. Salvador*[1], *Osman M. Bakr*[2], *Thomas D. Anthopoulos*[1], *Mario Lanza*[3], *Omar F. Mohammed*[2], *Frédéric Laquai*[1], *Stefaan De Wolf* [1*]

[1]KAUST Solar Center (KSC), Division of Physical Sciences and Engineering (PSE), King Abdullah University of Science and Technology (KAUST), Thuwal, 23955-6900, Kingdom of Saudi Arabia
[2]Advanced Membranes and Porous Materials Center (AMPMC) & KAUST Catalysis Center (KCC), Division of Physical Sciences and Engineering (PSE), King Abdullah University of Science and Technology (KAUST), Thuwal, 23955-6900, Kingdom of Saudi Arabia
[3]Division of Physical Sciences and Engineering (PSE), King Abdullah University of Science and Technology (KAUST), Thuwal, 23955-6900, Kingdom of Saudi Arabia

[*]Corresponding author email: jiang.liu@kaust.edu.sa; stefaan.dewolf@kaust.edu.sa

SUMMARY

Stacking perovskite solar cells onto crystalline-silicon bottom cells in a monolithic tandem configuration enables power conversion efficiencies (*PCEs*) well above those of their single-junction counterparts. However, the state-of-the-art wide-bandgap perovskite films suffer from phase stability issue. Here, we show how carbazole as an additive to the perovskite-precursor solution can not only reduce nonradiative recombination losses, but perhaps more importantly, suppress phase segregation under moisture exposure and light illumination. This enables a stabilized *PCE* of 28.6% (independently certified at 28.2%) for a monolithic perovskite/silicon tandem solar cell over ~1 cm^2, and 27.1% over 3.8 cm^2, built from a textured silicon heterojunction solar cell. The modified tandem devices retain ~93% of their performances over 43 days in a hot and humid outdoor environment, almost 100% over 250 h under continuous 1-sun illumination, and about 87% during 85-85 damp heat test for 500 h, demonstrating the improved phase stability.

Keywords: Perovskite/silicon tandem; Self-assembled monolayer; Passivation; Phase segregation; Stability; Outdoor testing

INTRODUCTION

Over the past decade, metal halide perovskites have triggered immense research activities in the photovoltaics (PVs) field[1-3]. Their band gap tunability, processing flexibility, and excellent optoelectronic properties make them an ideal sub-cell candidate for tandem applications, specifically when paired with mainstream crystalline silicon (c-Si) PVs[4-6]. Owing to their high absorption coefficient and low voltage loss, perovskite top cells can reduce the thermalization losses in the blue portion of the solar spectrum, relative to a narrower bandgap single junction c-Si cell, and enable *PCEs* of tandem beyond the single-junction limits[6,7]. High-efficiency perovskite/silicon tandem devices can be realized by tuning the perovskite top-cell band gap (E_g) to a value of 1.65-1.70 eV, where the ideal value may vary considering the field operation temperature and possible parasitic optical losses in the device layer stack[8-17]. Utilizing such perovskites as top-cell absorber, paired with silicon heterojunction (SHJ) bottom cells, perovskite/silicon tandem solar cells have been realized with *PCE* up to 29.5%[18], which is already well beyond the best-reported single-junction silicon heterojunction bottom cells[19,20].

To achieve a high-efficiency of such devices with long-term operational stability, implementing a phase-stable wide-bandgap perovskites is imperative[21]. However, to date, wide-bandgap metal halide perovskites (*i.e.* where E_g >1.65 eV) have been associated with considerable device phase-stability issues[22,23]. Many efforts such as via compositional engineering[24-26], crystallinity control[27-

[29], and defect passivation[30-32], have been devoted in the past few years to not only suppress the phase segregation issue of wide-bandgap perovskites, but also reduce the nonradiative recombination loss. For instance, increasing the Cs and reducing the Br concentrations, or adopting triple-halides in the perovskite for a target bandgap have been demonstrated as effective strategies to stabilize the perovskite layer under illumination.[25,26] However, a high Cs concentration in the perovskite precursor solution usually results in a poor film morphology and deteriorated electronic properties, possibly due to induced stresses in the resulting films[33,34]. Several earlier reports show that improved crystallinity and reduced trap densities render perovskite films to be more stable against halide segregation under illumination[27-29]. In addition, grain boundaries (GBs) accommodate a significant amount of charged defects due to the ionic nature of the perovskite film[35-37]. The passivation of trap states via some specific additives inside the precursor, such as theophylline[38], imidazolium[39], piperidinium[40] and some amine salts[31,32], has been reported as an effective strategy to circumvent this issue[30,31]. In these approaches, molecular passivation deactivates some defects via coordinate binding, and hence, reduces non-radiative recombination and improves photostability. Inspired by this, we incorporated carbazole as an additive into the perovskite precursor, and found that this additive can passivate deep charge traps, enhance performance, and suppress phase segregation of wide-bandgap perovskites. We find that this organic nitrogen-containing heterocyclic molecule interacts with halide anions through hydrogen bonds, immobilizes halide species and passivates trap states. Specifically, this happens at the GBs since the carbazole molecules with a relatively large molecular radius cannot be incorporated into the perovskite lattice. Combining this enhancement with minimized optical losses, we demonstrate a record-certified PCE of 28.2% for double-side textured perovskite/silicon tandems among openly published results. Equally important, passivating the defects at GBs inhibits ion migration within

the perovskite film and improves the long-term stability of the tandem device. The carbazole-treated tandem device retains over 93% of their initial performance for more than 40 days when tested outdoors, which demonstrates the improved phase stability of the wide-bandgap perovskites.

RESULTS AND DISCUSSION

Improved phase stability with carbazole additive

We performed systematic photoluminescence (PL) measurements to understand the role of the carbazole additive on the halide segregation in our 1.68 eV perovskites with a composition of $Cs_{0.05}FA_{0.8}MA_{0.15}Pb(I_{0.75}Br_{0.25})_3$. We confirmed the bandgap of our perovskite layer from a Tauc plot and the PL peak position (**Figure S1**). To exclude the influence of environmental factors such as humidity and oxygen[41], we encapsulated the samples in a nitrogen glove box. Under 1-sun equivalent illumination, we did not observe a significant change in the PL peak position within 15 min for both pristine and carbazole-treated samples (**Figure S2)**. However, this does not guarantee that these perovskite films will remain stable under long-term operation. To accelerate the degradation test, we increased the light intensity to 10 suns (**Figure 1A, B**). In that case, the pristine film shows an obvious extra peak in its lower-energy region, which gradually increases with irradiation time, indicating the formation of some light-induced I-rich trap states in the pristine film[25,42]. Notably, the carbazole-treated sample is much less affected, suggesting improved phase stability. Halide segregation of wide-bandgap perovskite films commonly occurs at GBs, activated by strain[23]. We speculate that carbazole molecules most probably stay at the GBs due to their incompatible size to fit the perovskite lattice. Thus, we can preliminarily infer that the introduction of carbazole additives to the perovskite precursor solution can hinder the migration of ions in the film, thereby suppressing halide segregation.

We further investigated the influence of ambient air on phase stability, and thus performed PL measurements on unencapsulated samples exposed to ambient air (RH ~55%). Clearly, exposure to humidity accelerates phase segregation (**Figure 1C**), especially for the control sample. When the pristine film was exposed to ambient air under dark for about three days, the re-measured PL spectrum shows a significant red-shift, while the carbazole-treated film was much less affected, implying enhanced phase-stability even under humid conditions. In addition, we also found that the synergistic effect of light and humidity will accelerate phase segregation (**Figure S3**). Our results show that the illumination intensity, the environmental atmosphere and trap-passivation all alter the dynamics of halide segregation. In the case of superposition of multiple stressors, halide segregation occurs faster, but the addition of carbazole minimizes this behavior.

To gain insight into the activation energy (E_a) of ion migration in the perovskite layer, temperature-dependent conductivity measurements were carried out (**Figure 1D**). The E_a for the pristine and carbazole-treated perovskite films were calculated to be 0.38 and 0.77 eV in the activation region (>260 K), respectively. Theoretical calculations have predicted that the halide ions are the most mobile ions in the perovskite films since they have the lowest activation energy[43]. Thus, the measured E_a here can mainly be linked to that for halide migration. The obvious increase in E_a after carbazole treatment offers quantitative evidence for additive-suppressed ion migration, which may be attributed to the bonding effect of carbazole at the GBs.

We performed conductive atomic force microscopy (c-AFM) measurements to study the conductivity difference between the grains and the GBs, potentially induced by the carbazole treatment. The topographic and current maps collected for both samples (see **Figure 1E,F** and

Figure S4) clearly indicate that the GBs have different conductivity compared to the grains. In the whole grain area, the carbazole-treated sample seems to have a lower current than the pristine one, which may be attributed to the higher bulk resistance of the carbazole-treated film. The more important information for this characterization is the difference in conductivity between the grain surface and the grain boundary. The line profile in Figure S4 clearly shows that for the carbazole-treated sample, most of GB regions show a lower current compared to their surrounding grain region, which could be attributed to the suppression of ion migration by carbazole at the GBs. However, for the control sample, the GB region exhibits a higher dark conductivity than the grain surface, indicating a higher ion migration activity at the GBs, which is also consistent with previous results that GBs can act as a channel for ion migration[44].

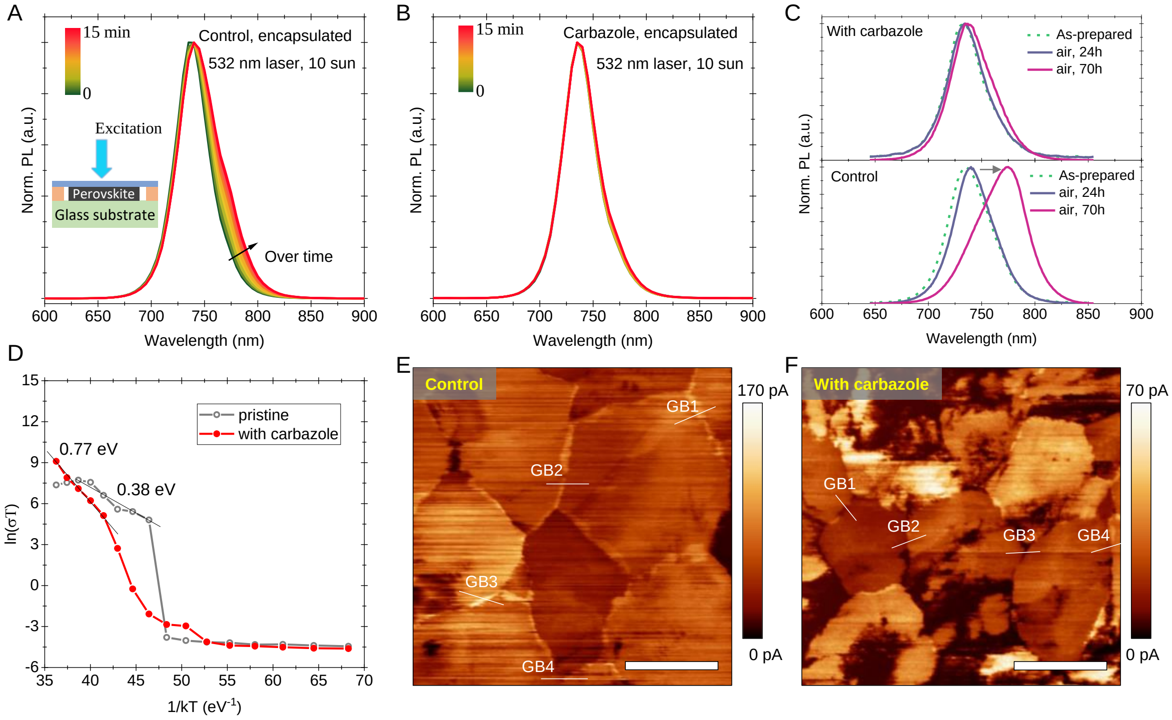

Figure 1. Phase stability and ion migration characterization of perovskite films. (A, B) Evolution of time-dependent photoluminescence spectra under 10 sun-equivalent laser illumination for (A) the control and (B) carbazole-treated encapsulated perovskite films. (C) Evolution of steady-state PL spectra for the

unencapsulated pristine films and carbazole-treated films upon exposure to air. (D) The temperature-dependent conductivity of the pristine film and carbazole-treated film. (E, F) c-AFM images of the perovskite films without and with carbazole, each of them with four grain boundaries (GB) indicated with white lines. Scale bar is 200 nm.

Mechanism of carbazole grain boundary passivation

In order to investigate the interaction between the carbazole and the perovskite, we conducted Fourier transform infrared (FTIR) spectroscopy. In **Figure 2A**, the absorption peak of the pure carbazole sample at around 3416, 1597 and 1449 cm^{-1} could be attributed to N-H stretching, N-H related bending, and C-N stretching frequencies, respectively[45]. For the carbazole-PbI_2 sample, the C-N stretching feature did not show any major shift in frequency, while the N-H stretching and N-H related bending vibrations shifted to 3410 and 1602 cm^{-1}, respectively, indicating that carbazole could interact with the perovskite through N-H bonding. We show the possible interaction mechanism of carbazole at the GBs of perovskites in **Figure 2C**.

In addition, we performed density functional theory (DFT) calculations on carbazole/perovskite interfacial models to further understand the role of carbazole on passivating the perovskite surface, as well as the atomistic interaction between them. Based on the X-ray diffraction (XRD) patterns (**Figure S7**), we considered three representative (100), (101) and (111) perovskite surfaces with different terminations and estimated the binding affinities of carbazole with these surfaces (all the optimized perovskite slab structures before and after carbazole adsorption are shown in **Figures S5** and **S6**). **Figure 2B** illustrates the carbazole/perovskite interfacial structures, where the perovskite surfaces are terminated with an outermost I or FAI layer. We find that the carbazole molecule is inclined to bind with surface I^- ions *via* hydrogen bonding (*i.e.*, N-H···I, 2.73 to 2.92 Å), where such interactions result in binding energies (E_b) in the range of -0.4 to -0.7 eV for FAI-rich (100) and I-rich (111) surfaces, respectively. For the I-rich (101) surface, a shorter hydrogen bond length (2.60 Å) as well as a larger E_b value (-2.26 eV) for the carbazole adsorption is found, suggesting that the carbazole molecules can stabilize the perovskite surface through hydrogen bonding interactions with halide ions, preventing halide ion migration from the surface into the bulk.

To demonstrate the passivation effect of this additive, time-resolved photoluminescence (TRPL) measurements were carried out (**Figure 2D**). The perovskite films with carbazole additive on both PTAA and 2PACz-based substrates exhibit a prolonged average PL decay time τ_{ave}, which improved from 910 to 1403 ns in the case of 2PACz. These results indicate that nonradiative recombination is significantly suppressed upon the addition of carbazole, which is expected to benefit the open-circuit voltage (V_{oc}) and fill factor (*FF*) of the tandem device. We also investigated the electronic properties of our perovskite films upon carbazole additive via contactless Terahertz (THz) spectroscopy (**Figure 2E**). The extracted yield-mobility product ($\varphi\Sigma\mu$) generally decreases with increasing carrier density. At the lowest photoinduced carrier densities (~1.6×10^{18} cm^{-3}), the pristine film shows a $\varphi\Sigma\mu$ mobility of around 22.1 $\mathrm{cm}^2\ \mathrm{V}^{-1}\ \mathrm{s}^{-1}$; this value increases to 25.8 for 0.25 mol%, 24.6 $\mathrm{cm}^2\ \mathrm{V}^{-1}\ \mathrm{s}^{-1}$ for 1 mol% sample. Combining the charge lifetime τ_{ave} from TRPL results and the average mobility $\varphi\Sigma\mu/2$ (**Table S1**), we can calculate the charge diffusion length L to be 5.1 and 6.8 μm for the pristine and passivated films, respectively, which are noticeably longer than the thickness of the absorber in the devices. The improved carrier diffusion length in the perovskite film, which is the result of largely suppressed trap density, can benefit charge collection. In addition, we also performed Hall-effect measurements (Table S2). Both films exhibit a very weak p-type conductivity. The pristine films show a hole mobility of 32.3 $\mathrm{cm}^2\ \mathrm{V}^{-1}\ \mathrm{s}^{-1}$ under 1 T magnetic field, which is slightly higher than the results obtained with

THz spectroscopy, while the carbazole-treated film show a relative increase of 13% to 39.0 cm^2 V^{-1} s^{-1}.

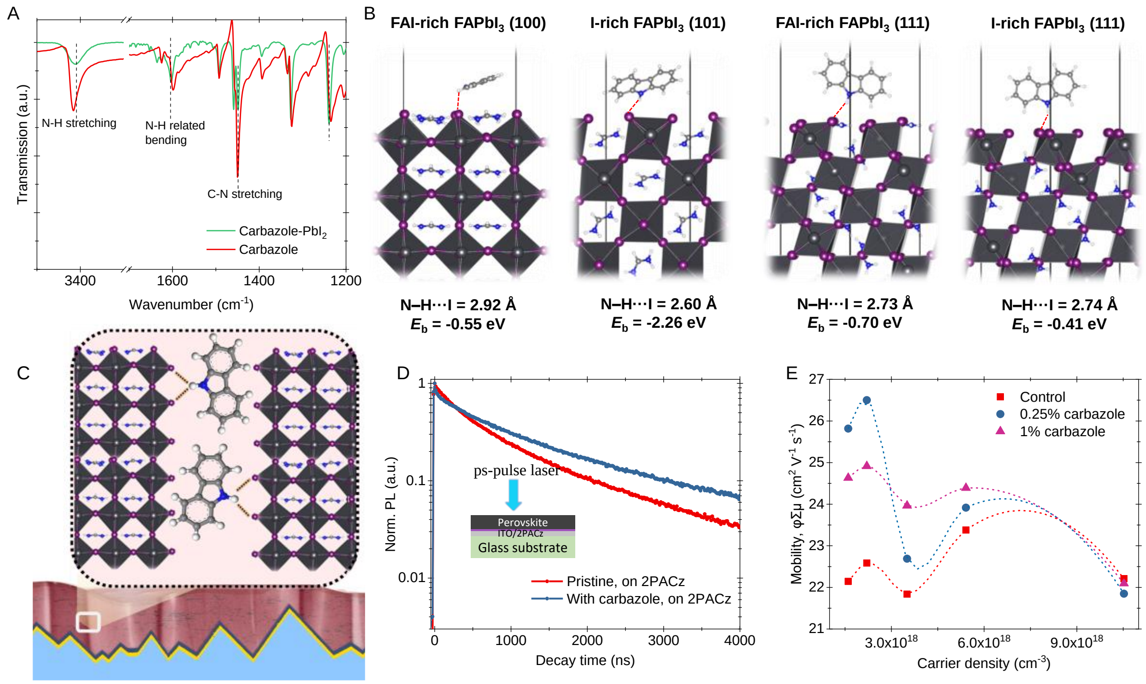

Figure 2. Mechanism of the grain boundary passivation with carbazole additive. (A) FTIR spectroscopy of pure carazole and cabazole-PbI$_2$ films. (B) Optimized interfacial structures for carbazole/FAPbI$_3$ models with different surface orientations and terminations of FAPbI$_3$, together with hydrogen bond lengths (red dashed lines) and binding energies (E_b) between carbazole and perovskite. (C) Schematic illustration of interaction of carbazole with perovskite films. (D) Time-resolved photoluminescence (TRPL) spectra of the wide-bandgap (1.68 eV) perovskite films with or without carbazole on 2PACz-coated ITO glass substrate. (E) Mobility as a function of excitation carrier density, extracted from Terahertz spectroscopy (TS).

Role of carbazole additive on the performance of single-junction devices

We first optimized the carbazole additive concentration on single-junction perovskite devices. For this, we fabricated *p-i-n* devices with glass/ITO/2PACz/1.68 eV perovskite/LiF/C$_{60}$/BCP/Ag configuration. To obtain micrometer thick perovskites, similar as those used on textured Si bottom cells in our tandem, we used here concentrated perovskite precursors (1.7 M), which results in a ~900 nm perovskite layer on a planar substrate (**Figure S12**). Such thick films provided a test platform to optimize the carbazole additives for subsequent application to tandem devices. The best single-junction current-voltage (*J-V*) curves under forward and reverse scans are shown in **Figure 3A**, and the photovoltaic parameters are listed in **Table S3**. The 2PACz-based control device shows a *PCE* of 19.2% with a V_{oc} of 1.21 V, a *FF* of 0.79. With carbazole treatment, the device exhibited a V_{oc} of 1.22 V, a short-circuit current density (J_{sc}) of 20.6 $\mathrm{mA{\cdot}cm^{-2}}$, and an *FF* of 0.81, yielding a *PCE* of 20.2%. The statistical PCE results (**Figure 3B** and **Figure S13**) demonstrate the reproducibility of the performance improvement after a small amount of carbazole addition was used. Clearly, the improvement mainly comes from V_{oc} and *FF*, which we attribute to the suppressed non-radiative recombination, as also supported by the TRPL results in **Figure 2C**. The built-in potential change upon carbazole addition has been evaluated by the Mott-Schottky analysis (**Figure S16**). Compared with the control device, the carbazole-treated device shows a shift toward higher cutoff voltage, indicating a higher flat-band potential, which is also consistent with improved V_{oc} after carbazole treatment.

To further demonstrate the minimized carrier recombination upon carbazole treatment, we obtained the dependence of the V_{oc} on the light intensity, as shown in **Figure 3C**. From the semi-logarithmic plot, we can find a linear relationship, following the expression $slope = \frac{nkT}{q} log_{10}e$, where n is the diode quality factor. The control and carbazole-treated devices exhibit an n value of 1.86 and 1.74, respectively. The lower n value indicates that trap-assisted recombination was suppressed in the carbazole-treated device. On the device level, we demonstrated the reduced defect density at the GBs via temperature-dependent admittance spectroscopy measurements

(**Figure 3D**). The capacitance distortion (Figure S17) mainly occurs at the frequency range of 10 to 1000 Hz, in which the defect densities could be derived. In order to avoid the influence of ion migration on the derived trap density, no any preconditioning was applied, and the device was in a zero bias and dark state environment during the measurement. The trap density of states (*tDOS*) analysis shows that at 300 K, the pristine device displays a peak trap density of 1.32×10^{17} cm^{-3} eV^{-1} at 0.44 eV, while the passivated device has a smaller peak intensity of 1.23×10^{17} cm^{-3} eV^{-1} at 0.39 eV.

We also carried out absolute photoluminescence (PL) imaging on the two perovskite devices under 1 sun light illumination. Following the previously established process[46,47], the absolute PL image could be converted into quasi-Fermi level splitting (*QFLS*) and Urbach energy (E_u) mapping (**Figure 3E, F** and **Figure S18**). The carbazole-passivated devices exhibit a slightly higher and narrower *QFLS* distribution than the control, with their statistical mean value of 1.20 and 1.19 eV, respectively. The *QFLS* directly reflects the internal voltage of the complete devices, and it is indeed remarkably close to the V_{oc} obtained from the 1-sun J-V curves. Ultraviolet photoelectron spectroscopy (UPS) results confirmed that the work function (*WF*) shifted down from 5.07 to 5.22 eV upon carbazole treatment (**Figure S10**), which could enable a higher internal voltage and more effective electron transfer at the interface between *ETL* and perovskite layer. In addition, the E_u distribution map with a mean value of 16.2 meV (**Figure S18**) was also obtained for the control sample, while the mean value for the carbazole-passivated sample is about 15.8 meV. The relatively larger *QFLS* and smaller E_u for carbazole-passivated devices provide further evidences for suppressed non-radiative recombination.

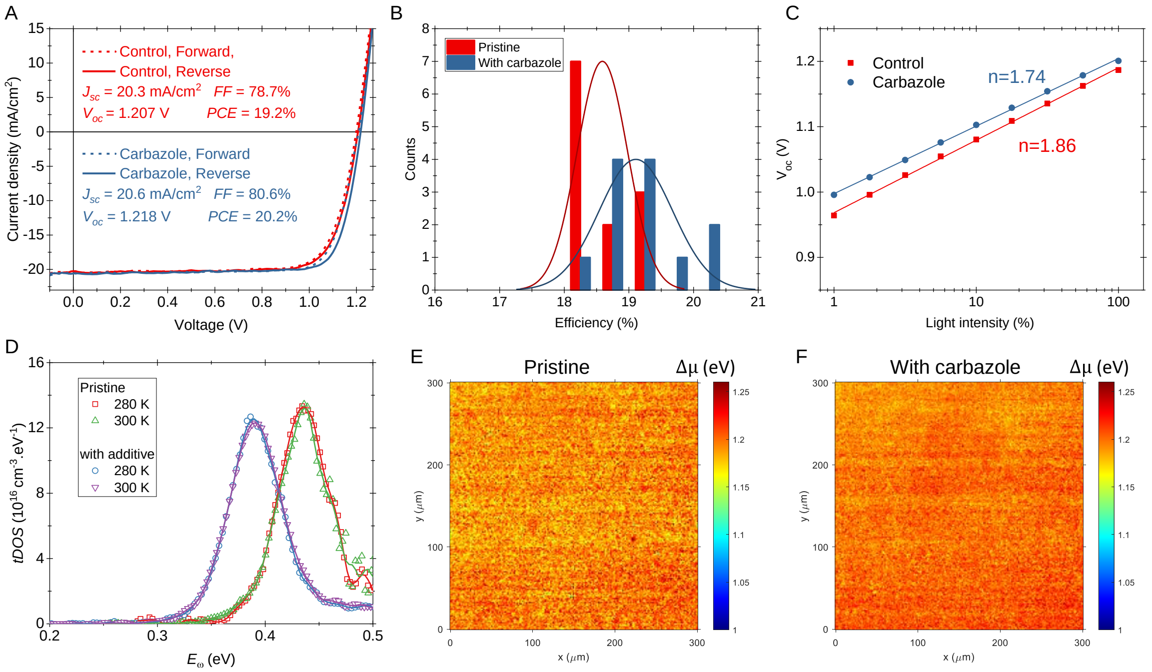

Figure 3. **Single-junction device performance.** (A) *J-V* curves of the champion 2PACz-based perovskite devices with or without carbazole treatment. (B) The statistics of *PCE* distribution. (C) V_{oc} evolution as a function of light intensities for the control and carbazole-treated perovskite devices. (D) Trap density of states (*tDOS*) distribution deduced from temperature-dependent C-f plots for the pristine and carbazole-treated devices. (E, F) Quasi-Fermi level splitting (*QFLS*) mapping for the ITO/2PACz/1.68 eV perovskite/LiF/C_{60} samples on glass under 1 sun equivalent light intensity.

Monolithic tandem device performance

After verifying our results in the single-junction platforms, we applied our carbazole-modified 1.68 eV perovskites on double-side textured silicon heterojunction bottom cells in the form of a tandem device. The schematic diagram of the device structure and the corresponding band structure are sketched in **Figure 4A** and **Figure S19**, respectively. Our Si bottom cell is mildly textured with a relative small pyramid size (Figure S27), so that our nearly-micron thick perovskite layer can cover the pyramid structure. The cross-section SEM image (Figure S20) of our tandem device shows our perovskite deposition technique provides end-to-end coverage. Previous optical simulations and experimental works[12,13,48] have shown that conformal coated perovskite on the textured bottom cells is an ideal structure. However, front-end flat devices fabricated on double-side mildly textured bottom cells still provide promising optical gain, as we demonstrated here. In our tandem devices, the conformal coated 2PACz layers on 20 nm ITO layers act as the recombination junction. **Figure 4B** shows the *J*-*V* characteristic of the champion perovskite/Si tandem device under an aperture area of 1.03 cm^2. The inset displays the photovoltaic parameters for the champion device, with a PCE of 28.9% and negligible *J*-*V* hysteresis. From MPP measurements with the 3-point perturbation method, we recorded a stabilized PCE of 28.6%, with a V_{MPP} of 1.58 V (**Figure 4C**). We verified the reproducibility of our processes, finding a narrow statistical distribution, as given in the inset in **Figure 4C,** acquired from 14 devices of multiple processing batches. The corresponding external quantum efficiency (*EQE*) spectra for this champion tandem device were obtained, as shown in **Figure S21**. The integrated photocurrent density was calculated to be 19.70 and 19.95 mA/cm^2, for perovskite and silicon subcells, respectively, which are in good agreement with the J_{sc} values from the *J*-*V* scan curve. The calculated spectral mismatch (see Supplementary note 4) for our tandem is 1.0163 for top cell, and 0.9799 for bottom cell. We verified our in-house measurements with 28.2% stabilized power output certified by an accredited laboratory (JET, Japan Electrical Safety & Environment Technology Laboratories) (**Figure S23)**. Our tandem device is commensurate with the state-of-the-art tandem devices in literature and represents the record-certified *PCE* for double-textured perovskite/Si tandem devices (**Table S4**). Importantly, our tandem device shows a relatively high J_{sc} value, by taking the advantage of improved light management in double-side textured bottom cell structures. The relatively large refractive index difference between the Si and perovskite layer generally causes a considerable reflectance from the overall device. Applying a random-pyramid textured structure at the top side of the Si bottom cell increases the optical light path and reduces the reflectance loss. To demonstrate the superiority of the double-textured structure in terms of light-harvesting, we compared the EQE and reflectance of the perovskite subcell on planar and textured Si substrates (**Figure S24**). Clearly, the textured structure significantly reduces the light reflectance in the response region of the c-Si subcell, as evidenced by the reflection curve in **Figure S24**. A certain percentage of photons at the band edge of the perovskite layer (wavelength of 580 to 720 nm) still could transmit through the perovskite cell to reach the Si bottom cell. With our highly crystalline micrometer thick perovskite, the photon utilization of the perovskite subcell near the band edge was also greatly improved.

We showed the scalability potential of our tandem devices on a larger substrate with an aperture area of 3.8 cm^2. A best *PCE* of 27.1% under reverse scan was achieved, as shown in **Figure 4E**. The V_{oc} of this device reached 1.88 V, even slightly higher than that of our ~1 cm^2 area devices. Based on the respective performance results of perovskite and silicon single-junction devices (**Figure S26 and 27**), the V_{oc} contribution from perovskite and Si subcell may be ~1.19 and ~0.69 V, respectively. The EQE spectra (**Figure 4I**) from three different spots show that the integrated J_{sc} is within a range of ±0.08 mA/cm^2. All these findings confirm the uniformity of our devices on larger substrates. The absolute ~3% *FF* and 0.5 mA/cm^2 J_{sc} losses between ~1 cm^2 and ~3.8 cm^2 devices are due to the relatively large series resistance of evaporated silver contacts, and additional shading losses of the silver fingers. We expect that the utilization of industrially compatible screen-printed Ag contact can help reduce these electrical losses, which is considered as a future study.

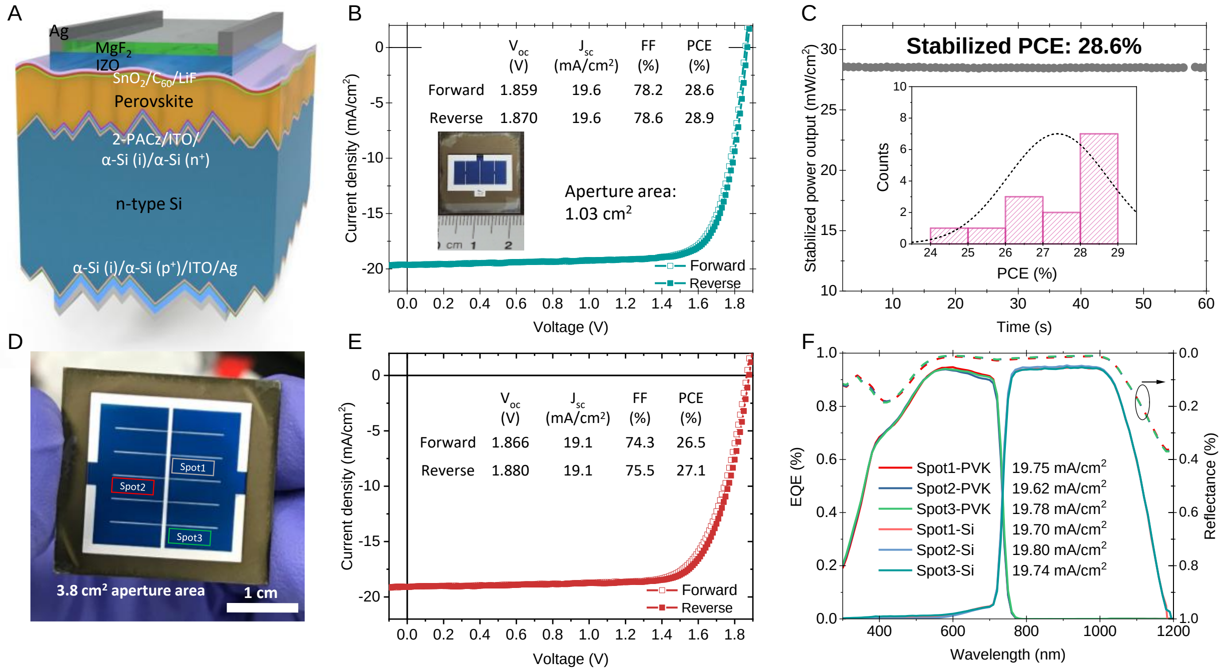

Figure 4. **Tandem device performance.** (A) Schematic of the textured monolithic perovskite/Si tandem device. (B) J-V curves of the champion tandem cell with an aperture area of 1.03 cm^2. The inset shows the photo of the corresponding device. The substrate size is around 23 mm*23 mm. (C) Stabilized power output of the champion tandem device at the maximum power point (*MPP*) under AM 1.5G illumination. The inset is the statistics of PCE distribution for our tandem devices fabricated in several batches. (D) The photo of the tandem device with an aperture area of 3.8 cm^2. (E) J-V curves of the champion 3.8 cm^2 tandem device. (F) EQE spectra from three different spots on one tandem device.

Stability evaluation

To evaluate the effect of the carbazole additive on the stability of our tandem devices, we carried out a series of tests on encapsulated devices under different environmental conditions, including outdoor and continuous light soaking tests, as well as 85 ^{o}C/85% IEC 61215:2016 (also called ISOS-D3) damp heat tests. Specifically, 43 days outdoor testing in a hot and sunny desert climate (see photo in **Figure S29**) includes all quadrants of the operational conditions such as continuous operation under illumination and heat, and heat cycles from day to night. The daily peak device temperature can reach above 45 ^{o}C (**Figure S30**) and the light intensity on a sunny day can reach

0.95 suns (measured by a pyranometer) at noon. These conditions represent an ideal test platform to understand the real-world behavior of tandem devices at a targeted operational location, such as for large solar energy plants. For better comparison, the daily performance evolution of the pristine device (dashed grey line) is superimposed on that of the carbazole-treated device (colored fill areas) in **Figure 5A**. On the sub-graph of the short-circuit current (I_{sc}), the two devices show an almost coinciding trend. However, the daily peak V_{oc} and power output (P_m) trend curves gradually diverge with the passing of time. Clearly, the carbazole-treated device exhibits superior stability compared with the control. For the carbazole-treated device, on the first day (23-Nov-2020), the peak P_m value and the corresponding light intensity was 18.2 mW/cm^2 and 0.937 sun, yielding a *PCE* of 19.4% (**Table S5**). After 38 days of outdoor testing, the P_m can reach 19.3 mW/cm^2 under 1.015 sun, potentially implying the *PCE* retention could reach almost 98% if it is assumed that the spectrum on the 38th day is almost the same as that on the first day. In contrast, the control device shows a faster decay in performance, with the power output decreasing from 17.7 mW/cm^2 initially to 13.0 mW/cm^2 and the *PCE* from 19% to 14.6% after 40 days. To demonstrate the change in photovoltaic performance on the first day and the 38th day, Figure S31 shows the J-V curves recorded each ~10 min under forward scan from 7 am to 6 pm. Depending on the intensity and distribution of the daily spectrum, the daily *PCE* or retention shows some fluctuations. Overall, after 40 days of outdoor testing, the performance retention reaches over 93% for the carbazole-treated device, while it is only about 77% for the control device. The performance degradation in the pristine device was mainly from the decrease in V_{oc}, possibly indicating the degradation in this field test was from perovskite itself. These results could demonstrate that the carbazole additive can improve the stability of tandem devices under light and heat stress.

We further carried out the operational stability evaluation of tandem devices in a controlled lab environment under continuous Xenon-lamp illumination with MPP tracking (**Figure 5B**). After 250 h, the reference device showed about 8% performance loss. In contrast, our carbazole-treated device retained nearly 100% of the initial performance. The main difference between the two devices is in the initial few hours of the aging process, which may be associated with a rapid increase in the density of trap states for the pristine device. The bias during the aging process may cause ion migration and promote the generation of some trap defects, which especially occurred in the initial aging process. In the subsequent aging process, the trap state density may be favorably stabilized at the GBs or at the interfaces, and accordingly, the performance would be relatively stable. Therefore, we can infer that the defect formation rate in the reference device was faster than that in the carbazole-treated one.

To demonstrate the tolerance of our encapsulated devices to high temperature and high humidity environments, we performed a damp heat test at 85 ^{o}C with 85% relative humidity (**Figure 5C** and **Figure S32**). Notably, after nearly 500 hours, the V_{oc} and J_{sc} in our tandems were quite stable, and the *PCE* retention could reach up to 87%. The performance degradation mainly was found in the *FF*, which could be associated with degraded top contact electrode. The highly stable V_{oc} implies that the perovskite layer itself did not degrade after 500 h of damp heat testing. We can speculate that as the testing time progressed, the degradation in our damp heat test should be due to moisture invasion rather than inherent thermal decomposition.

After the long-term stability test, the cross-sectional morphology of the tandem devices was characterized. The devices were taken out by deliberately destroying the encapsulation glass. For the carbazole-treated device after several-months of outdoor test, we couldn’t observe an obvious change in the cross-sectional SEM images (**Figure S33**). The PL mappings (**Figure 5D, E**) on two tandem devices were obtained. For the pristine device, significant phase segregation could be observed in the range of hundreds of microns, possibly implying irreversible degradation. Based on the PL spectra (**Figure 5F**), some narrow bandgap (<1.68 eV) regions appeared in a large areal portion; these regions show a stronger PL intensity because the iodine-rich phase primarily acts as a recombination trap[32,49]. In contrast, such phase segregation was not observed in the carbazole-treated devices after outdoor testing, as evidenced by the uniform distribution of PL spectra in **Figure S34**. These results confirm that the carbazole treatment suppressed phase segregation, thus improving the long-term operational stability of the tandem devices.

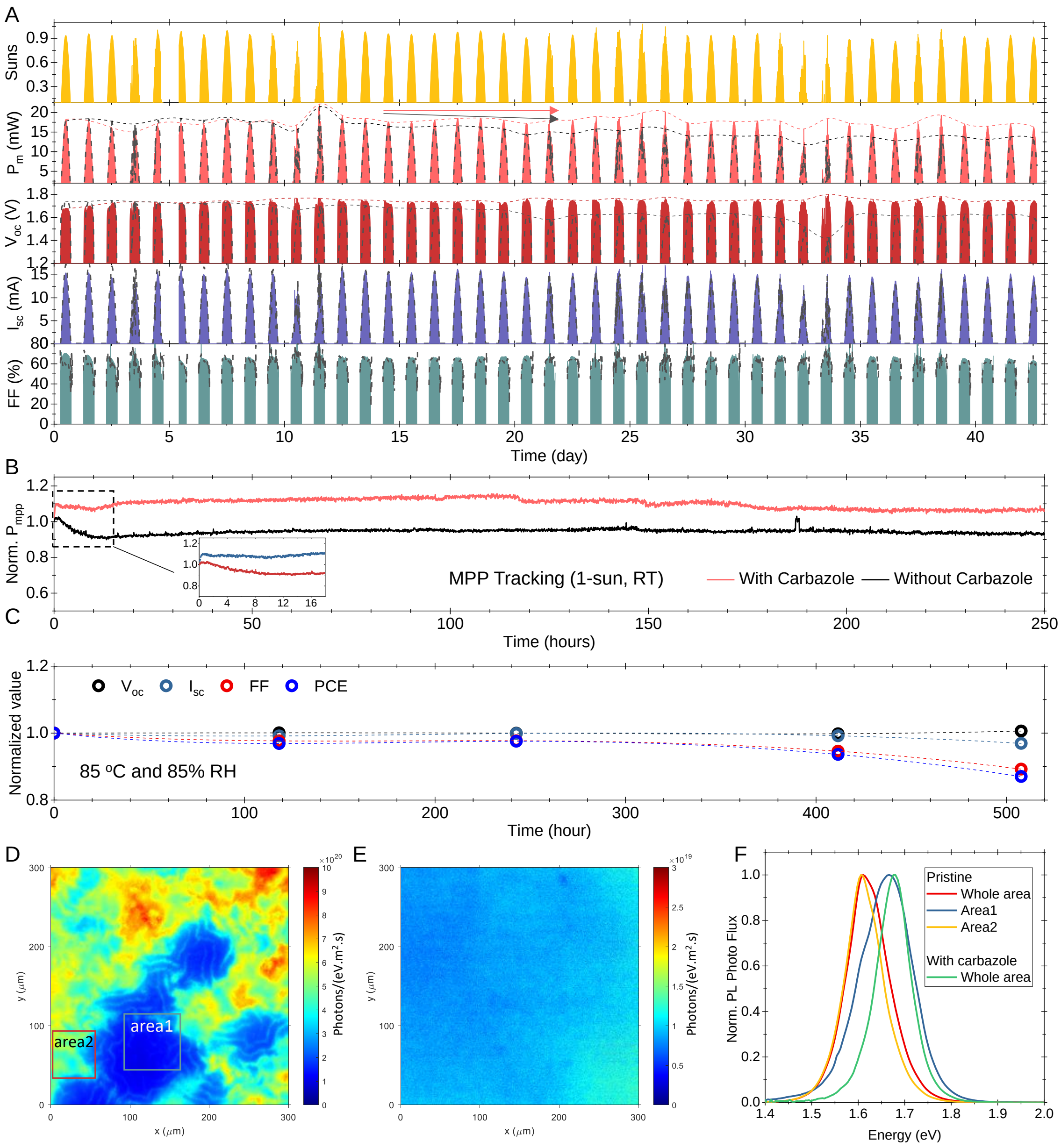

Figure 5. **Stability analysis of the tandem devices.** (A) Outdoor performance of the tandem device in a hot desert climate, measured at KAUST campus (location: Thuwal, Jeddah, Saudi Arabia) for 43 days. J-V scans under forward direction were performed approximately every 10 min during the daytime. The colored fill areas represent the results of the carbazole-treated encapsulated tandem device, while the dashed grey line in photovoltaic parameters data represents that of the pristine device without additive. 1 sun indicates 100 mW/cm^2 solar irradiance. The daily maximum values of V_{oc} and P_m are connected by dotted lines in an interpolated manner. (B) Long-term MPP tracking of the tandem devices with and without carbazole, under continuous Xenon light illumination. (C) Photovoltaic performance evolution of one encapsulated tandem device which was subjected to a damp-heat environment at 85 °C and 85% relative humidity (RH). (D, E) Absolute PL intensity mapping at 1.68 eV under 1-sun light illumination for the encapsulated (D) control and (E) carbazole-treated devices after outdoor tests. (F) PL spectra of the device on different positions.

Conclusions

We demonstrated that the addition of carbazole could suppress phase segregation under light and humid air stress, and passivate the perovskite films, leading to a significant reduction in the density of trap states. After integrating our optimized wide-bandgap perovskite cell onto a silicon heterojunction bottom cell, we achieved a certified 28.2%-efficient monolithic perovskite/silicon tandem device. A series of stability tests on encapsulated tandem devices were carried out to prove the durability of our tandem devices, showing that the carbazole additive leads to a significant improvement in device stability even in a hot and humid outdoor environment. Our work demonstrates great prospects for future practical applications of perovskite/Si tandem solar cells. A further understanding of the passivation characteristics of additives in perovskite films will likely be essential for the development of efficient and stable perovskite-silicon tandem solar cells.

AUTHOR INFORMATION

Corresponding Authors
*Email: Jiang.liu@kaust.edu.sa (J.L)
*E-mail: stefaan.dewolf@kaust.edu (S.D.W.).
Jiang Liu: 0000-0001-9933-0218
Erkan Aydin: 0000-0002-8849-2788
Michele De Bastiani: 0000-0002-4870-2699
Stefaan De Wolf: 0000-0003-1619-9061

Conflict of Interest

The authors declare no conflict of interest.

Acknowledgements

This work was supported by the King Abdullah University of Science and Technology (KAUST) Office of Sponsored Research (OSR) under Award No: OSR-CARF URF/1/3079-33-01, KAUST OSR-CRG 400 RF/1/3383, KAUST OSR-CRG2018-3737.

AUTHOR CONTRIBUTIONS

Jiang Liu conceived and conducted the research. Jiang Liu and Erkan Aydin wrote the paper. Jun Yin performed DFT calculation. Michele De Bastiani, Atteq ur Rehman and Thomas G. Allen fabricated the Si bottom cell. Emre Yengel performed the Ion-migration activation energy measurement. Esma Ugur helped to conduct PL measurement. George T. Harrison performed XPS measurement. Mingcong Wang and Yajun Gao performed THz and PDS measurement. Jafar I Khan contributed to TRPL data analysis. Michele De Bastiani and Maxime Babics encapsulated the tandem cells. Furkan H. Isikgor, Anand S. Subbiah, Xiaopeng Zheng, Wenbo Yan and Fuzong Xu contributed to data analysis. Michael F. Salvador contributed to outdoor tests. Kaichen Zhu and Mario Lanza performed AFM measurement. Osman M. Bakr, Thomas D. Anthopoulos, Mario Lanza, Omar F. Mohammed, Frédéric Laquai, Stefaan De Wolf Supervised the project and contributed to manuscript draft.

References

1 Kojima, A., Teshima, K., Shirai, Y. & Miyasaka, T. (2009). Organometal Halide Perovskites as Visible-Light Sensitizers for Photovoltaic Cells. J. Am. Chem. Soc. *131*, 6050-6051.

2 Lee, M. M., Teuscher, J., Miyasaka, T., Murakami, T. N. & Snaith, H. J. (2012). Efficient hybrid solar cells based on meso-superstructured organometal halide perovskites. Science *338*, 643-647.

3 Jeon, N. J., Noh, J. H., Kim, Y. C., Yang, W. S., Ryu, S. & Seok, S. I. (2014). Solvent engineering for high-performance inorganic-organic hybrid perovskite solar cells. Nat. Mater. *13*, 897-903.

4 De Bastiani, M., Subbiah, A. S., Aydin, E., Isikgor, F. H., Allen, T. G. & De Wolf, S. (2020). Recombination junctions for efficient monolithic perovskite-based tandem solar cells: physical principles, properties, processing and prospects. Mater. Horiz. *7*, 2791-2809.

5 Werner, J., Niesen, B. & Ballif, C. (2018). Perovskite/Silicon Tandem Solar Cells: Marriage of Convenience or True Love Story? - An Overview. Adv. Mater. Interfaces *5*, 1700731.

6 Leijtens, T., Bush, K. A., Prasanna, R. & McGehee, M. D. (2018). Opportunities and challenges for tandem solar cells using metal halide perovskite semiconductors. Nat. Energy *3*, 828-838.

7 Lal, N. N., Dkhissi, Y., Li, W., Hou, Q., Cheng, Y.-B. & Bach, U. (2017). Perovskite Tandem Solar Cells. Adv. Energy Mater. *7*, 1602761.

8 Mazzarella, L., Lin, Y. H., Kirner, S., Morales-Vilches, A. B., Korte, L., Albrecht, S., Crossland, E., Stannowski, B., Case, C., Snaith, H. J. et al. (2019). Infrared Light Management Using a Nanocrystalline Silicon Oxide Interlayer in Monolithic Perovskite/Silicon Heterojunction Tandem Solar Cells with Efficiency above 25%. Adv. Energy Mater. *9*, 1803241.

9 Kim, D., Jung, H. J., Park, I. J., Larson, B. W., Dunfield, S. P., Xiao, C., Kim, J., Tong, J., Boonmongkolras, P., Ji, S. G. et al. (2020). Efficient, stable silicon tandem cells enabled by anion-engineered wide-bandgap perovskites. Science *368*, 155-160.

10 Chen, B., Yu, Z., Liu, K., Zheng, X., Liu, Y., Shi, J., Spronk, D., Rudd, P. N., Holman, Z. & Huang, J. (2019). Grain Engineering for Perovskite/Silicon Monolithic Tandem Solar Cells with Efficiency of 25.4%. Joule *3*, 177-190.

11 Chen, B., Yu, Z. S. J., Manzoor, S., Wang, S., Weigand, W., Yu, Z. H., Yang, G., Ni, Z. Y., Dai, X. Z., Holman, Z. C. et al. (2020). Blade-Coated Perovskites on Textured Silicon for 26%-Efficient Monolithic Perovskite/Silicon Tandem Solar Cells. Joule *4*, 850-864.

12 Sahli, F., Werner, J., Kamino, B. A., Brauninger, M., Monnard, R., Paviet-Salomon, B., Barraud, L., Ding, L., Diaz Leon, J. J., Sacchetto, D. et al. (2018). Fully textured monolithic perovskite/silicon tandem solar cells with 25.2% power conversion efficiency. Nat. Mater. *17*, 820-826.

13 Aydin, E., Allen, T. G., De Bastiani, M., Xu, L. J., Avila, J., Salvador, M., Van Kerschaver, E. & De Wolf, S. (2020). Interplay between temperature and bandgap energies on the outdoor performance of perovskite/silicon tandem solar cells. Nat. Energy *5*, 851-859.

14 Hou, Y., Aydin, E., De Bastiani, M., Xiao, C., Isikgor, F. H., Xue, D.-J., Chen, B., Chen, H., Bahrami, B., Chowdhury, A. H. et al. (2020). Efficient tandem solar cells with solution-processed perovskite on textured crystalline silicon. Science *367*, 1135-1140.

15 Al-Ashouri, A., Kohnen, E., Li, B., Magomedov, A., Hempel, H., Caprioglio, P., Marquez, J. A., Morales Vilches, A. B., Kasparavicius, E., Smith, J. A. et al. (2020). Monolithic perovskite/silicon tandem solar cell with >29% efficiency by enhanced hole extraction. Science *370*, 1300-1309.

16 Aydin, E., Liu, J., Ugur, E., Azmi, R., Harrison, G. T., Hou, Y., Chen, B., Zhumagali, S., De Bastiani, M., Wang, M. et al. (2021). Ligand-bridged charge extraction and enhanced quantum efficiency enable efficient n-i-p perovskite/silicon tandem solar cells. Energy Environ. Sci., 10.1039/d1031ee01206a.

17 Bush, K. A., Palmstrom, A. F., Yu, Z. J., Boccard, M., Cheacharoen, R., Mailoa, J. P., McMeekin, D. P., Hoye, R. L. Z., Bailie, C. D., Leijtens, T. et al. (2017). 23.6%-efficient monolithic perovskite/silicon tandem solar cells with improved stability. Nat. Energy *2*, 17009.

18 NREL, Best Research-Cell Efficiency Chart, https://www.nrel.gov/pv/cell-efficiency.html.

19 Allen, T. G., Bullock, J., Yang, X., Javey, A. & De Wolf, S. (2019). Passivating contacts for crystalline silicon solar cells. Nat. Energy *4*, 914-928.

20 Yoshikawa, K., Kawasaki, H., Yoshida, W., Irie, T., Konishi, K., Nakano, K., Uto, T., Adachi, D., Kanematsu, M., Uzu, H. et al. (2017). Silicon heterojunction solar cell with interdigitated back contacts for a photoconversion efficiency over 26%. Nat. Energy *2*, 17032.

21 Knight, A. J. & Herz, L. M. (2020). Preventing phase segregation in mixed-halide perovskites: a perspective. Energy Environ. Sci. *13*, 2024-2046.

22 Hoke, E. T., Slotcavage, D. J., Dohner, E. R., Bowring, A. R., Karunadasa, H. I. & McGehee, M. D. (2015). Reversible photo-induced trap formation in mixed-halide hybrid perovskites for photovoltaics. Chem. Sci. *6*, 613-617.

23 Zhao, Y., Miao, P., Elia, J., Hu, H., Wang, X., Heumueller, T., Hou, Y., Matt, G. J., Osvet, A., Chen, Y. T. et al. (2020). Strain-activated light-induced halide segregation in mixed-halide perovskite solids. Nat. Commun. *11*, 6328.

24 Duong, T., Pham, H., Kho, T. C., Phang, P., Fong, K. C., Yan, D., Yin, Y., Peng, J., Mahmud, M. A., Gharibzadeh, S. et al. (2020). High Efficiency Perovskite ‐ Silicon Tandem Solar Cells: Effect of Surface Coating versus Bulk Incorporation of 2D Perovskite. Adv. Energy Mater. *10*, 1903553.

25 Xu, J., Boyd, C. C., Yu, Z. J., Palmstrom, A. F., Witter, D. J., Larson, B. W., France, R. M., Werner, J., Harvey, S. P., Wolf, E. J. et al. (2020). Triple-halide wide-band gap perovskites with suppressed phase segregation for efficient tandems. Science *367*, 1097-1104.

26 Bush, K. A., Frohna, K., Prasanna, R., Beal, R. E., Leijtens, T., Swifter, S. A. & McGehee, M. D. (2018). Compositional Engineering for Efficient Wide Band Gap Perovskites with Improved Stability to Photoinduced Phase Segregation. ACS Energy Letters *3*, 428-435.

27 Rehman, W., McMeekin, D. P., Patel, J. B., Milot, R. L., Johnston, M. B., Snaith, H. J. & Herz, L. M. (2017). Photovoltaic mixed-cation lead mixed-halide perovskites: links between crystallinity, photo-stability and electronic properties. Energy Environ. Sci. *10*, 361-369.

28 Zhou, Y., Jia, Y.-H., Fang, H.-H., Loi, M. A., Xie, F.-Y., Gong, L., Qin, M.-C., Lu, X.-H., Wong, C.-P. & Zhao, N. (2018). Composition-Tuned Wide Bandgap Perovskites: From Grain Engineering to Stability and Performance Improvement. Adv. Funct. Mater. *28*, 1803130.

29 Braly, I. L., Stoddard, R. J., Rajagopal, A., Uhl, A. R., Katahara, J. K., Jen, A. K. Y. & Hillhouse, H. W. (2017). Current-Induced Phase Segregation in Mixed Halide Hybrid Perovskites and its Impact on Two-Terminal Tandem Solar Cell Design. ACS Energy Lett. *2*, 1841-1847.

30 Abdi-Jalebi, M., Andaji-Garmaroudi, Z., Cacovich, S., Stavrakas, C., Philippe, B., Richter, J. M., Alsari, M., Booker, E. P., Hutter, E. M., Pearson, A. J. et al. (2018). Maximizing and stabilizing luminescence from halide perovskites with potassium passivation. Nature *555*, 497-501.

31 Zhou, Y., Wang, F., Cao, Y., Wang, J.-P., Fang, H.-H., Loi, M. A., Zhao, N. & Wong, C.-P. (2017). Benzylamine-Treated Wide-Bandgap Perovskite with High Thermal-Photostability and Photovoltaic Performance. Adv. Energy Mater. *7*, 1701048.

32 Isikgor, F. H., Furlan, F., Liu, J., Ugur, E., Eswaran, M. K., Subbiah, A. S., Yengel, E., De Bastiani, M., Harrison, G. T., Zhumagali, S. et al. (2021). Concurrent cationic and anionic perovskite defect passivation enables 27.4% perovskite/silicon tandems with suppression of halide segregation. Joule *5*, 1566-1586.

33 Bush, K. A., Rolston, N., Gold-Parker, A., Manzoor, S., Hausele, J., Yu, Z. J., Raiford, J. A., Cheacharoen, R., Holman, Z. C., Toney, M. F. et al. (2018). Controlling Thin-Film Stress and Wrinkling during Perovskite Film Formation. ACS Energy Lett. *3*, 1225-1232.

34 Turren-Cruz, S. H., Hagfeldt, A. & Saliba, M. (2018). Methylammonium-free, high-performance, and stable perovskite solar cells on a planar architecture. Science *362*, 449-453.

35 Chen, B., Rudd, P. N., Yang, S., Yuan, Y. & Huang, J. (2019). Imperfections and their passivation in halide perovskite solar cells. Chem. Soc. Rev. *48*, 3842-3867.

36 Yang, S., Dai, J., Yu, Z., Shao, Y., Zhou, Y., Xiao, X., Zeng, X. C. & Huang, J. (2019). Tailoring Passivation Molecular Structures for Extremely Small Open-Circuit Voltage Loss in Perovskite Solar Cells. J. Am. Chem. Soc. *141*, 5781-5787.

37 Aydin, E., De Bastiani, M. & De Wolf, S. (2019). Defect and Contact Passivation for Perovskite Solar Cells. Adv. Mater. *31*, e1900428.

38 Wang, R., Xue, J., Wang, K. L., Wang, Z. K., Luo, Y., Fenning, D., Xu, G., Nuryyeva, S., Huang, T., Zhao, Y. et al. (2019). Constructive molecular configurations for surface-defect passivation of perovskite photovoltaics. Science *366*, 1509-1513.

39 Bai, S., Da, P., Li, C., Wang, Z., Yuan, Z., Fu, F., Kawecki, M., Liu, X., Sakai, N., Wang, J. T. et al. (2019). Planar perovskite solar cells with long-term stability using ionic liquid additives. Nature *571*, 245-250.

40 Lin, Y. H., Sakai, N., Da, P., Wu, J., Sansom, H. C., Ramadan, A. J., Mahesh, S., Liu, J., Oliver, R. D. J., Lim, J. et al. (2020). A piperidinium salt stabilizes efficient metal-halide perovskite solar cells. Science *369*, 96-102.

41 Ugur, E., Alarousu, E., Khan, J. I., Vlk, A., Aydin, E., De Bastiani, M., Balawi, A. H., Gonzalez Lopez, S. P., Ledinský, M., De Wolf, S. et al. (2020). How Humidity and Light Exposure Change the Photophysics of Metal Halide Perovskite Solar Cells. Solar RRL *4*, 2000382.

42 Belisle, R. A., Bush, K. A., Bertoluzzi, L., Gold-Parker, A., Toney, M. F. & McGehee, M. D. (2018). Impact of Surfaces on Photoinduced Halide Segregation in Mixed-Halide Perovskites. ACS Energy Lett. *3*, 2694-2700.

43 Eames, C., Frost, J. M., Barnes, P. R., O'Regan, B. C., Walsh, A. & Islam, M. S. (2015). Ionic transport in hybrid lead iodide perovskite solar cells. Nat. Commun. *6*, 7497.

44 Yuan, Y. & Huang, J. (2016). Ion Migration in Organometal Trihalide Perovskite and Its Impact on Photovoltaic Efficiency and Stability. Acc. Chem. Res. *49*, 286-293.

45 Jana, S., Kumar Trivedi, M. & Branton, A. (2015). Physical and Structural Characterization of Biofield Energy Treated Carbazole. Pharm. Anal. Acta *6*, 1000435.

46 Stolterfoht, M., Wolff, C. M., Márquez, J. A., Zhang, S., Hages, C. J., Rothhardt, D., Albrecht, S., Burn, P. L., Meredith, P., Unold, T. et al. (2018). Visualization and suppression of interfacial recombination for high-efficiency large-area pin perovskite solar cells. Nat. Energy *3*, 847-854.

47 Braly, I. L., deQuilettes, D. W., Pazos-Outón, L. M., Burke, S., Ziffer, M. E., Ginger, D. S. & Hillhouse, H. W. (2018). Hybrid perovskite films approaching the radiative limit with over 90% photoluminescence quantum efficiency. Nat. Photonics *12*, 355-361.

48 Santbergen, R., Mishima, R., Meguro, T., Hino, M., Uzu, H., Blanker, J., Yamamoto, K. & Zeman, M. (2016). Minimizing optical losses in monolithic perovskite/c-Si tandem solar cells with a flat top cell. Opt Express *24*, A1288-1299.

49 Caprioglio, P., Caicedo-Dávila, S., Yang, T. C.-J., Wolff, C. M., Peña-Camargo, F., Fiala, P., Rech, B., Ballif, C., Abou-Ras, D., Stolterfoht, M. et al. (2021). Nano-emitting Heterostructures Violate Optical Reciprocity and Enable Efficient Photoluminescence in Halide-Segregated Methylammonium-Free Wide Bandgap Perovskites. ACS Energy Lett. *6*, 419-428.

50 Zhao, J., Deng, Y., Wei, H., Zheng, X., Yu, Z., Shao, Y., Shield, J. E. & Huang, J. (2017). Strained hybrid perovskite thin films and their impact on the intrinsic stability of perovskite solar cells. Sci. Adv. *3*, eaao5616.

51 Kresse, G. & Furthmuller, J. (1996). Efficient iterative schemes for ab initio total-energy calculations using a plane-wave basis set. Phys. Rev. B *54*, 11169-11186.

52 Kresse, G. & Joubert, D. (1999). From ultrasoft pseudopotentials to the projector augmented-wave method. Phys. Rev. B *59*, 1758-1775.

EXPERIMENTAL PROCEDURES

Materials

Patterned tin-doped indium oxide (ITO) (~15 Ω/sq) coated glass was purchased from Xin Yan Technology LTD. Lead iodide (PbI_2) and lead bromide ($PbBr_2$) were purchased from Alfa Aesar. Formamidinium iodide (FAI), methylammonium bromide (MABr) were purchased from Greatcell Solar. Cesium iodide (CsI), anhydrous dimethylformamide (DMF), anhydrous dimethyl sulfoxide (DMSO), anhydrous chlorobenzene (CB), lithium fluoride (LiF), Carbazole were purchased from Sigma-Aldrich. PTAA was bought from Xi'an p-OLED. [2-(9H-carbazol-9-yl)ethyl]phosphonic acid (2PACz) was purchased from TCI. C_{60} (>99.5% purity) was purchased from Nano-C. Bathocuproine (BCP, >99.5% purity) was bought from Ossila Ltd. The ceramic 2-inch IZO target was purchased from Plasmaterials, Inc. All the chemicals were used as received without further purification.

Si bottom cell fabrication

4-inch *n*-doped float-zone (FZ) Si wafer with a thickness of 260-280 μm was used for Si bottom cell fabrication. The double-side texture structure with random distributed pyramids was obtained using an alkaline solution. The size of the pyramids is controlled by adjusting the alkaline concentration and the process temperature. The wafers were dipped in hydrofluoric acid solution followed by cleaning process, before transferred into a plasma enhanced chemical vapour deposition (PECVD) cluster (Indeotec Octopus II) for amorphous silicon (α-Si) deposition. 8 nm intrinsic (i), 6 nm n-doped, and 13 nm p-doped α-Si layer were grown on wafer using the PECVD cluster tool. The process temperatures are 200 °C. The power for i-a-Si:H layer deposition is 50 W with a 800 sccm H_2 and 25 sccm SiH_4. The n-doped α-Si layer was deposited under 40 W with 15 sccm SiH_4 and 92 sccm 2% PH_3/H_2, and the p-doped α-Si layer was deposited under 40 W with 50 sccm SiH_4 and 75 sccm 2% Trimethylborane/H_2. 150 nm ITO and 250 nm Ag were sputtered on the backside of the wafer. 15 nm ITO recombination junction was sputtered on the front side. In order to recover sputtering damage, an annealing step at 200 °C for 10 min was carried out.

Single-junction perovskite solar cell fabrication

ITO glasses were ultrasonically cleaned with detergent, deionized water, acetone, and isopropanol successively, and then blow-dried with compressed nitrogen. The substrates were subjected to UV-Ozone treatment for 15 min before any film deposition. For PTAA deposition, 2 mg/mL PTAA solution in CB was used. For 2PACz deposition, 1 mg/mL 2-PACz in ethanol was used. The 2PACz molecule can covalently bind to the underlying ITO layer through its phosphonic acid anchoring group, thereby forming a conformal self-assembled monolayer. The PTAA or 2PACz as hole transport layer (HTL) was spin-coated on ITO-coated substrates at 5000 rpm for 50 s, followed by drying at 100 °C for 10 min. 1.7 M $Cs_{0.05}FA_{0.8}MA_{0.15}Pb(I_{0.75}Br_{0.25})_3$ perovskite precursor solution was prepared by dissolving a mixture of FAI, MABr, CsI, PbI_2, and $PbBr_2$ in a mixed solvent (DMF/DMSO = 4:1). A certain amount of carbazole was added into the perovskite solution. A low spin coating speed with a relatively long dwell time is beneficial to obtain a complete coverage of perovskite layer on the textured silicon cells. The perovskite films were spin-coated at 2000 rpm for 50 s then followed with 7000 rpm for 10 s. Chlorobenzene was dropped in the center of the substrates 12 s before the end of the spin-coating process. After the rotation ceased, the substrates were immediately transferred onto a hotplate of 100 °C and were annealed for 15 min. 1 nm LiF, 25 nm C_{60}, 6 nm BCP and 100 nm Ag layers were thermally evaporated on perovskite films sequentially.

Perovskite top cell fabrication on Si substrate

The Si bottom wafers were subjected to UV-Ozone treatment for 15 min before transferred into the glovebox. The processes for HTL and perovskite deposition is the same as that on single-junction devices. After perovskite deposition, 1 nm LiF and 15 nm C_{60} were subsequently deposited by thermal evaporation. 20 nm SnO_2 was then deposited by atomic layer deposition (ALD) using a Picosun system. The substrate temperature was maintained at 100 ^oC during ALD deposition with TDMASn precursor source at 80 ^oC and H_2O source at 18 ^oC. The pulse and purge time for Tetrakis(dimethylamino)tin(IV) (TDMASn) is 1.6 and 5.0 s with a 90 sccm carrier gas of nitrogen, for H_2O is 1.0 and 5.0 s with 90 sccm N_2. 140 cycles was used. For IZO deposition, a 3-inch IZO ceramic target containing 98 wt% In2O3 and 2 wt% ZnO was used. 25 sccm Ar with 0.5% O_2 was used a process gas, yielding a ~0.5 mTorr process pressure. 70 nm IZO was sputtered on top of the SnO_2 through a shadow mask using a 43 W sputtering power. Ag finger with a thickness of 350 nm was thermally evaporated using a high precision shadow mask. Finally, 120 nm MgF_2 was thermally evaporated as an anti-reflection layer. The thickness of LiF, C_{60}, IZO and MgF_2 layers were first calibrated by spectroscopic ellipsometer. The evaporation rate and thickness of each experiment were monitored by quartz crystal microbalance sensors.

Device encapsulation and stability tests

The tandem devices were sandwiched between two cover glasses with black butyl rubber sealant at the edges. Tinned plated copper strips were used to contact the upper and lower electrodes of the tandem devices using Ag paste, and extend to the outside of the cover glass. For outdoor stability measurement, the encapsulated devices were mounted at KAUST campus in a hot desert climate, with a tilt angle of 25° and south-facing orientation. Devices were masked with a black tape, and J-V scans were performed approximately every 10 min during the daytime. The solar irradiance was recorded using a calibrated pyranometer. Data acquisition was performed using EKO's MP160 software. For indoor stability measurement, the encapsulated devices were placed on a metal plate with a controlled temperature of 25 °C. The devices were continuously exposed to white light generated by Xenon lamp of Newport solar simulator, and were tracked at MPP using a home-made software. For damp heat test, the devices were placed inside an environmental chamber with a condition of 85 ^{o}C and 85% relative humidity, and were taken out for J-V measurement at some intervals.

Solar cell Characterization:

Single-junction opaque devices were tested in a glove box using Keithley 2400 at room temperature under AM 1.5G illuminations (1000 W/m^2) from an Abet Technologies Sun 3000 solar simulator which was calibrated using a standard silicon cell (RERA). Current-voltage (J-V) curves were obtained both in reverse (1.3 V → -0.1 V) and forward scan (-0.1 V → 1.3 V) with a step size of 10 mV. J-V measurements on tandem devices were performed in the air under LED-based solar simulator (Wavelabs Sinus 220). About 200 mV/s scan speed was used and no preconditioning was used in this work. A mask with an aperture area of 1.03 cm^2 for tandem device was used. The light intensity was calibrated using Fraunhofer ISE CalLab certified c-Si solar cells. EQE measurements were measured using a LOANA system (PV-Tools). The chopped monochromatic light beam was focused entirely on the active area of the solar cells. When measuring Si bottom subcell, a blue LED light (525 nm) was illuminated on the cell and a 0.6 V bias voltages were applied. When measuring perovskite top subcell, a near-infrared LED (950 nm) was illuminated on the cell and a 0.9 V bias voltages were applied.

Atomic force microscopy measurement

Current and topographic mappings were obtained using a Digital Instruments Multimode AFM (Veeco Metrology Group). Current mappings were obtained using PeakForce TUNA mode. AFM tips (model: PFTUNA) with nominal tip radius 25 nm, nominal spring constant 0.4 N/m and 20 nm PtIr coating. The perovskite films were deposited on ITO-coated glass substrate. A voltage of 1 V was applied to the substrate and the tip was grounded.

Photoluminescence measurement

Steady photoluminescence (PL) and time-resolved photoluminescence (TRPL) measurements were carried out with a spectrofluorometer (Fluoroma-Modular, Horiba Scientific). For steady PL, 500 nm monochromatic light was continuously illuminated on the surface of the films. Emission spectra with wavelengths between 650 nm and 850 nm were collected. For TRPL, a 633 nm pulsed laser which was generated from a picosecond laser diode (PicoQuant) was used for the pump excitation. The fluence is estimated to be around ~10 nJ/cm^2. A long-pass 650 nm filter was used, and 738 nm light was probed.

For time-dependent photoluminescence spectra measurement, the perovskite films on bare glass were encapsulated in a nitrogen glovebox using an ultra-thin glass cover slide with edge sealed by UV-curable epoxy. The PL spectra was recorded about each 1 min using hyperspectral luminescence imaging system equipped with an optical microscope with a 20 X objective and a 532 nm laser with controlled laser intensity.

Terahertz spectroscopy (TS) measurement

Upon light excitation, the non-equilibrium photo-generated free charge will cause the conductivity change (ΔS) in the perovskite film, which causes changes in THz transmission. A relationship may be expressed as

$$\Delta S = \varepsilon_0 c(n_A + n_B)(\frac{\Delta T}{T})$$

Where ΔT is the photo-induced change in terahertz electric field. n_A and n_B are the refractive index of the perovskite film and quartz substrate. The number of photo-excited charge carriers N was determined using

$$N = \Phi \frac{E}{h\nu} Abs$$

where E is the total energy of the excitation pulse, $h\nu$ is photon energy, Abs is the absorptivity of the sample to the excitation light. Φ is the ratio of charges created per photon absorbed.

The charge carrier mobility μ is given by

$$\mu = \Phi \frac{\Delta S A_{eff}}{Ne}$$

where A_{eff} is the overlapping area between the spots of optical pumping light and THz probe light.

Ion-migration activation energy measurement

The temperature-dependent conductivity measurement was carried out to extract ion-migration activation energy following previously established processes[50]. Laser scribing with a wavelength of 532 nm was first applied onto ITO-coated substrates, resulting in a scribing width of ~40 μm. Lateral devices were then fabricated by depositing perovskite layer on the patterned ITO substrates. The devices were placed inside a Lakeshore Probe Station under vacuum condition. The device was first cooled and stabilized at 170 K for 30 min. Then, the device was slowly heated to 320 K with a step of 10 K. A 50 V voltage was applied to the two insolated ITO electrodes, and current was collected after a stabilization time of 10 s. The activation energy for ion migration was extracted based on the following Nernst-Einstein equations:

$$\sigma(T) = \frac{\sigma_0}{T} \exp(-\frac{E_a}{kT})$$

where σ_0 and k are constants, σ and T are temperature-dependent conductivity and temperature, respectively, and E_a is the activation energy for ion migration. E_a can be derived from the slope of the ln(σT) versus 1/kT curves.

Trap density measurements by thermal admittance spectroscopy

Frequency-dependent capacitance measurement on complete devices was carried out at different temperature conditions. The density of the defect is given by the equation below

$$N_T(E_\omega) = -\frac{V_{bi}}{qW}\frac{dC}{d\omega}\frac{\omega}{k_B T}$$

$$E_\omega = k_B T \ln(\frac{\beta T^2}{\omega})$$

where V_{bi} denotes the built-in voltage in the junction, ω is the angular frequency, q is the elementary charge, k is the Boltzmann's constant, T is the temperature, E_ω is the demarcation energy, and β is a temperature independent parameter. Only the defects below the demarcation energy can follow the applied ac voltage, and the charging and discharging of the defect contribute to the capacitance.

Following the equation $\omega_0 = \beta T^2 \exp(-\frac{E_a}{kT})$, the defect activation energy (Ea) and β can be extracted from the slope and intercept of the $\ln(\omega_0/T^2)$ versus $1/kT$ curves. The characteristic transition frequency ω_0 can be determined by the extreme value of the capacitance spectrum derivative with respect to frequency (-*f**d*C*/d*f*).

Density functional theory (DFT) calculations

We performed density functional theory (DFT) calculations on the carbazole/$FAPbI_3$ interfaces by using the generalized gradient approximation (GGA) approach and the Perdew-Burke-Ernzerhof (PBE) functional as implemented in Vienna *ab initio* simulation package (VASP)[51,52]. The carbazole/$FAPbI_3$ interfacial models were built by placing carbazole molecules on both the top and bottom surfaces of $FAPbI_3$ slabs. We further relaxed the atomic positions until the total Hellmann-Feynman forces in each atom were less than 0.01 eV/Å. The cutoff energy of plane-wave basis set for the wavefunctions was set at 500 eV. The Uniform Brillouin zone grids of a 6×6×6 *k*-mesh for the cubic-phase $FAPbI_3$ bulk, a 4×4×1 *k*-mesh for the $FAPbI_3$ slabs and for the carbazole/$FAPbI_3$ interfaces were used. The binding energies (E_b) were calculated with the equation of $E_b = (E(\text{total}) - E(\text{FAPbI}_3) - E(\text{carbazole}))/2$, where E(total) is the total energy, E($FAPbI_3$) is the energy of $FAPbI_3$ slab, and E(carbazole) is the energy of carbazole molecule.